Title
Investigating magnetic susceptibility of human knee joint at 7 Tesla

Journal
Magnetic Resonance in Medicine, 78(5)

ISSN
0740-3194

Authors
Wei, Hongjiang
Dibb, Russell
Decker, Kyle
et al.

Publication Date
2017-11-01

DOI
10.1002/mrm.26596

Peer reviewed

HHS Public Access

Author manuscript

Magn Reson Med. Author manuscript; available in PMC 2018 November 01.

Published in final edited form as:

Magn Reson Med. 2017 November ; 78(5): 1933–1943. doi:10.1002/mrm.26596.

Investigating Magnetic Susceptibility of Human Knee Joint at 7 Tesla

Hongjiang Wei, PhD[1,2], **Russell Dibb**[3], **Kyle Decker**[3], **Nian Wang, PhD**[1], **Yuyao Zhang, PhD**[1,2], **Xiaopeng Zong, PhD**[4], **Weili Lin, PhD**[4,5], **Daniel B. Nissman, MD, MPH, MSEE**[4,5], and **Chunlei Liu, PhD**[1,2,6]

[1]Brain Imaging and Analysis Center, Duke University, Durham, NC, USA

[2]Department of Electrical Engineering and Computer Sciences, University of California, Berkeley, CA, USA.

[3]Center for In Vivo Microscopy, Duke University, Durham, NC, USA

[4]Department of Radiology, School of Medicine, University of North Carolina at Chapel Hill, Chapel Hill, NC, USA

[5]Biomedical Research Imaging Center, University of North Carolina at Chapel Hill, Chapel Hill, NC, USA

[6]Department of Radiology, School of Medicine, Duke University, Durham, NC, USA

Abstract

Purpose—To evaluate the magnetic susceptibility properties of different anatomical structures within the knee joint using quantitative susceptibility mapping (QSM).

Methods—A collagen tissue model was simulated and *ex vivo* animal cartilage experiments were conducted at 9.4 T to evaluate the B_0 orientation-dependent magnetic susceptibility contrast observed in cartilage. Furthermore, nine volunteers (six healthy subjects without knee pain history and three patients with known knee injury, age between 29 and 58 years) were scanned using gradient-echo acquisitions on a high-field (7 T) magnetic resonance (MR) scanner. Susceptibility values of different tissues were quantified and diseased cartilage and meniscus were compared against that of healthy volunteers.

Results—Simulation and *ex vivo* animal cartilage experiments demonstrated that collagen fibrils exhibit an anisotropic susceptibility. A gradual change of magnetic susceptibility was observed in the articular cartilage from the superficial zone to the deep zone, forming a multilayer ultra-structure consistent with anisotropy of collagen fibrils. Meniscal tears caused a clear reduction of susceptibility contrast between the injured meniscus and surrounding cartilage illustrated by a loss of the sharp boundaries between the two. Moreover, QSM showed more dramatic contrast in the focal degenerated articular cartilage than R2* mapping.

Correspondence Address: Chunlei Liu, Ph.D., Department of Electrical Engineering and ComputerSciences, and the Helen Wills Neuroscience Institute at the University of California, Berkeley. 505Cory Hall, Berkeley, CA94720, USA. Phone:(510)6647596, chunlei.liu@berkeley.edu.

Conclusion—The arrangement of the collagen fibrils is a significant and likely the most dominant source of magnetic susceptibility anisotropy. QSM offers a means to characterize magnetic susceptibility properties of tissues in the knee joint. QSM is sensitive to collagen damage or degeneration and may be useful for evaluating the status of knee diseases, such as meniscal tears and cartilage disease.

Keywords

Quantitative susceptibility mapping; cartilage; knee

Introduction

Magnetic susceptibility is an intrinsic physical property of a material and quantifies the strength of magnetization induced in that material when placed in an external magnetic field, e.g. the static magnetic B_0 field in MRI. Quantitative susceptibility mapping (QSM), solving the ill-posed inverse problem from field to susceptibility, allows extraction of the spatial distribution of the bulk magnetic susceptibility (1–6). QSM has been applied to assess iron deposits (7,8); probe the anisotropic structure of white matter in the brain (9–11), of tubules in the kidney (12), and of myofibers in the heart (13,14); distinguish diamagnetic calcium from paramagnetic iron (15,16); and image the cytoarchitecture of the whole mouse brain (17). Early studies have shown that QSM does show promise in the analysis of joint tissues (18–20) and cartilage canals (21,22). However, it has not been successfully applied for detecting human knee diseases. Previous studies (23) have shown that T2* mapping (that is influenced both by the transverse relaxation (T2) and by local susceptibility fields) can be used to assess the articular cartilage, which indicates a potential application of QSM in the knee diseases.

Various MRI techniques that are sensitive to collagen structure, water content, and proteoglycan content have been previously reported, e.g. diffusion tensor imaging (24), T2* mapping (23), and T1ρ (T1 relaxation time in the rotating frame) quantification (25). Although these techniques have shown promise for characterizing the cartilage matrix composition, knee disease is a multi-systemic disease (26), stemming from not only diseased articular cartilage, but also from disease in any type of joint tissues, including the subchondral bone, capsule, menisci, and even sciatic nerves. Each of these components has a unique cellular composition and microstructure and thus may exhibit varying magnetic susceptibility. QSM is particularly sensitive to molecular content, cellular arrangement and tissue microstructure (27–29), and therefore may be suitable to evaluate the microstructure changes throughout the knee joint. However, application of QSM in the knee is faced with an additional technical challenge not critical in the brain – the chemical shift due to fatty tissues. This chemical shift affects the complex MRI signal, particularly the phase signal and further the QSM quantification (19,20,30,31).

The purpose of this work is to evaluate the susceptibility properties of different anatomical structures of the knee and further to test QSM on patients with knee disease. We demonstrate that 1) intricate knee structures exhibit different magnetic susceptibility properties and values; 2) B_0 orientation-dependent collagen contrast exists in the cartilage; 3) QSM is able

to reveal the multilayer ultra-structures of articular cartilage; and 4) QSM may have the potential to provide assessment of meniscal and cartilage degeneration.

Methods

A Micro-structure model of a Collagen Fibril with Susceptibility Anisotropy

A microstructural model of collagen was developed to evaluate the contribution of the diamagnetic anisotropy of the peptide bonds on the B_0 orientation-dependent magnetic susceptibility in cartilage, as shown in Fig. 1. Collagen II is the major collagen in cartilage and comprises polypeptide chains in the form of left-handed polyproline II-type helices. These peptide group planes orient at approximately 45° to the fibril axis (32). Three parallel polyproline II-type chains wind together into a right-handed collagen-typical triple helix that is ~1–1.5 nm in diameter (33). The staggered assembly of five triple helices yields a microfibril segment (34). A structure of 14 microfibrils (a ring of 10 microfibrils surrounding a core of 4 microfibrils, or 10+4 for short) make up a complete collagen fibril (34).

A 64 × 64 × 64 voxel array with 0.3 nm isotropic resolution was simulated inside a volume. This resolution selection is based on axial spacing between peptides in the left-handed II-type helices (35). The collagen microfibrils with diameter of 4 nm are simulated and 10+4 model was constructed, producing a collagen fibril. The diameter of the fibril was 15 nm and the center-to-center microfibril spacing was 4 nm.

The simulation for calculation of the macroscopic susceptibility anisotropy with respect to B_0 was conducted following the procedure proposed by Dibb et al. (13). Each voxel within the volume that contains a peptide bond was assigned the same relative susceptibility tensor,

$$\chi=\chi_I \mathrm{I}+\begin{bmatrix} \chi_A & 0 & 0 \\ 0 & -\chi_{A/2} & 0 \\ 0 & 0 & -\chi_{A/2} \end{bmatrix} \quad (1)$$

where χ_A and χ_I represent the anisotropic and isotropic susceptibility values, respectively. Each of these tensors was rotated according to its position in the right-handed triple helix. Using the theoretical molar susceptibility anisotropy value calculated by Pauling, -5.36×10^{-6} cm^3/mol (CGS units) (36) and the simulated volume size. The model-specific volume susceptibility anisotropy of each voxel containing a peptide group was calculated as $\Delta\chi = \chi_{11} - (\chi_{22} + \chi_{33})/2 = -4.14$ ppm (SI units). The anisotropic susceptibility component, i.e. the magnetic susceptibility normal to the helix axis, was calculated, $\chi_A = \Delta\chi \times 2/3 = -2.76$ ppm. The isotropic susceptibility value of the peptide bond was calculated by fitting the simulation model to the measured apparent susceptibility values as described in the *ex vivo* experiments section. According to the angle (θ) between the simulated fibrils orientation and the static B_0 field ($\hat{\mathbf{H}}$), three-dimensional frequency maps for the model array (Δf) were simulated using tensor formulation of the susceptibility-frequency equation in the subject frame of reference (10),

$$\Delta f = FT^{-1}\left\{\left(\frac{1}{3}\hat{\mathbf{H}}^T FT\{\chi\}\hat{\mathbf{H}} - \hat{\mathbf{H}}^T \boldsymbol{k}\frac{\boldsymbol{k}^T FT\{\chi\}\hat{\mathbf{H}}}{k^2}\right) FT\{\chi\}\right\}\gamma\mu_0 H \quad (2)$$

Finally, a complex average of uniformly distributed spins across the entire 3D frequency map yield a complex signal. An estimate of the bulk susceptibility of a voxel containing collagen fibril tissue, χ, was calculated using the theoretical relationship $\Delta f/f_0 = \chi/3$ with the spherical inclusion correction (37), where f_0 is the resonance frequency. The simulation was then repeated for a range of collagen fibril orientations (0 – 90°) with respect to $\hat{\mathbf{H}}$ to model susceptibility anisotropy as a function of TE. Within a simulated volume, we calculated the spatially varying frequency perturbation and signal magnitude of spins within and outside the collagen fibril in the regions contained by the solid gray and dashed gray rectangle boxes respectively, shown in Fig. 3A.

Assessing Susceptibility Anisotropy using Animal Model

All animal preparation protocols were approved by the Duke University Institutional Animal Care and Use Committee. Fresh samples of two adult pig knee joints were obtained from a local abattoir. Pieces of articular cartilage were removed from the femoral cartilage using a surgical knife. The animal experiments were performed using a 9.4-T 8.9-cm vertical bore Oxford magnet controlled by an Agilent VnmrJ 4.0 console. Each cartilage specimen was firmly affixed in an 11-mm cylindrical polyethylene cartridge filled with Galden® (perfluoropolyether; Solvay Specialty Polymers) to provide a background without MR signal and susceptibility properties similar to that of water. The specimen cartridge was placed inside a sphere, allowing for an arbitrary specimen orientation inside the coil (12). Magnitude and phase data were acquired using a 3D GRE sequence with 18 echoes (TE_1/ΔTE/TE_{18} = 3/2/37 ms). TR = 150 ms, flip angle = 35°, matrix size = 150 × 150 × 150, isotropic voxel size = 100 μm, total scan time per orientation = 40 mins. The specimen was repositioned in a new orientation prior to every image acquisition. To assess the B_0 orientation dependence of the magnetic susceptibility, three image orientations were acquired for each specimen. The $\hat{\mathbf{H}}$ vectors for the three acquisitions were: (0, 0, 1), (−1, −0.05, 0.07) and (−0.7, −0.6, 0.36), which corresponds to 0°, 86° and 69° referenced to the normal of the articular surface, respectively. The raw data were unwrapped using Laplacian-based phase unwrapping (38). The background phase was removed using projection onto dipole fields (PDF) (39) and the magnetic susceptibility was determined by two-level STAR-QSM (streaking artifact reduction for QSM) algorithm (40).

Two small region of interests (ROI) were manually selected from the superficial layer (black rectangle in Fig. 4B) and deep layer (red rectangle in Fig. 4B) of the cartilage using the ITK-SNAP software (41). Within each ROI were tissue voxels with similarly orientated collagen fibrils, and the mean collagen fibril direction acquired at orientation [0 0 1] were approximately perpendicular and parallel to B_0 field for superficial zone (χ_{90}) and deep zone (χ_0), respectively. The mean apparent magnetic susceptibility within the ROIs were calculated. Then the isotropic susceptibility value of the peptide bond tensor, χ_I, was calculated by using the simulated model to fit the apparent susceptibility of specimen using

mean squared error minimizing algorithm that was weighted by the inverse of the standard deviation within each ROI (step size = 0.01 ppm).

Human Imaging Protocols and Study Participants

MR imaging was performed on the knee of nine volunteers (seven men and two women, aged between 29 and 58 years; six volunteers had no history of knee pain or surgery in either knee; three patients had meniscal tear or cartilage degeneration). Imaging was carried out with approval of the institutional review board and informed consent from the subjects, and in compliance with the Health Insurance Portability and Accountability Act. All images were acquired with a 7 T MRI scanner (Siemens Healthcare, Erlangen, Germany) located at UNC Biomedical Research Imaging Center using a dedicated 28-channel knee coil. Automated high-order shimming preceded all acquisitions. A sagittal 3D fast low-angle shot (FLASH) sequence was used to acquire images with the following parameters: TE_1/spacing/TE_4 = 2.12/2.2/8.72 ms, TR = 35 ms, flip angle = 15°, bandwidth = ±651 Hz/pixel, matrix size = 380 × 384 × 88, voxel size = 0.4 × 0.4 × 1.6 mm^3, frequency encoding in the superior-inferior direction, a parallel imaging method (GRAPPA) was used with a reduction factor of three, and total acquisition time was under 6 minutes per scan. The scan was repeated two more times with TE_1 increased by 0.3 ms between acquisitions, giving a total of three scans. Then the three scans were combined and used as input for the water-fat separation reconstruction.

The patients (Patient 1, 58-year-old male. Patient 2, 39-year-old male. Patient 3, 30-year-old female) were scanned with two additional sequences. A sagittal 3D proton density (PD) (turbo-spin-echo) sequence with fat saturation was applied with the following imaging parameters: TR/TE = 8170/14 ms, flip angle = 180°, bandwidth = ±132 Hz/pixel, matrix size = 380 × 384 × 36, voxel size = 0.4 × 0.4 × 3 mm^3. A sagittal T2 fast spin echo (FSE) sequence with fat saturation was applied with the following parameters: TR/TE = 4000/148 ms, flip angle = 120°, bandwidth = ±766 Hz/pixel, matrix size = 380 × 384 × 88, voxel size = 0.4 × 0.4 × 1.6 mm^3.

Data Reconstruction

Application of QSM in the knee joint faces a technical challenge: the presence of fat introduces a significant chemical shift which confounds the estimate of B_0 field map. In this study, the B_0 field map is estimated using a chemical shift encoded reconstruction (42). The local susceptibility distribution can be estimated from the measured B_0 field map without contamination by chemical shift. Moreover, we improve susceptibility map calculations with reduced streaking artifacts using a two-level regularization approach to reconstruct large and small susceptibility values (40,43). A schematic view of QSM reconstruction is shown in Figure 2. First, complex multi-echo images are used to estimate the B_0 field map, water and fat images (Fig. 2B). Second, the sum of squares of the magnitude images are used to obtain the mask (Fig. 2C), covering the knee joint while excluding the bone regions, by using a semi-automatic level-set based segmentation integrated in MIPAV software (NIH, Medical Image Processing, Analysis, and Visualization). This binary mask provides edge information to calculate the local field (Fig. 2D) by removing the background field using PDF (39). The

local field map is subsequently input to the two-level STAR-QSM algorithm (40,43) to obtain the QSM maps (Fig. 2E).

Data Analysis

The anatomical structure in the susceptibility maps were manually drawn using a Matlab-based region-of-interest (ROI) tool integrated in STISuite (http://people.duke.edu/~cl160/). Six major tissues were segmented, each labeled with different colors, the cartilage (label 1), muscle (label 2), tibial nerve (label 3), fat pad (label 4), menisci (label 5), and subcutaneous fat (label 6). The mean and standard deviation (SD) was calculated for each ROI. The one-way analysis of variance (ANOVA) with Post Hoc Tukey procedure was used to evaluate significance of difference between tissues which have the same susceptibility property, i.e. either paramagnetic or diamagnetic. All statistical analysis was performed using SPSS 21 (IBM, SPSS Inc., Chicago). $P < 0.05$ was considered to be statistically significant.

Meniscal tears and abnormal areas of cartilage were compared on PD, T2 FSE, and QSM images. Moreover, the abnormal areas within the medial side cartilage revealed by QSM were compared with normal healthy volunteers on GRE magnitude, R2* and further compared against the normal lateral side cartilage.

Results

Simulation Results

Using the mean apparent magnetic susceptibility within selected ROIs (shown in Fig. 4B) calculated from each individual GRE echo images, the simulated model computed a best-fit relative isotropic susceptibility value for the peptide group tensor ($\chi_I = 0.02$ ppm). Fig. 3C&E show that signal magnitude is orientation dependent and decays faster within intra-fibril space (within solid gray box) than extra-fibril space (within dashed gray box). Fig. 3D shows that the apparent frequency of a complex average of the solid gray box varies with time, and is strongly dependent on the fibril orientation relative to B_0 field. The complex average of distributed spins across the entire simulated volume yielded a TE-dependent frequency map (Fig. 3H). Fig. 3I compares the simulated anisotropy data to the experimental data on the *ex vivo* animal specimen. Both simulated and experimental data show that susceptibility anisotropy increases as TE increases. Susceptibility anisotropy reaches its plateau at TE around 8 ms.

Ex vivo Animal Results

R2* and QSM images measured at each orientation are shown in Fig. 4. The measured susceptibility contrast varies markedly between different orientations. The anisotropy in the cartilage collagen fibrils is clearly evident, and corresponds to the collagen fibril orientation with respect to the B_0 field. Contrarily, this B_0 field-orientation dependence appears relatively small from the R2* maps.

In vivo Human Knee Results

An example of a high resolution 3D GRE magnitude sagittal slice is shown in Fig. 5A. Several intricate structures and complex interfaces are visible, including body fat, tendons,

cartilages, fat pad, menisci, and muscles. Fig. 5B–C show a comparison of QSM maps obtained with (Fig. 5B) and without (Fig. 5C) the use of chemical shift removal reconstruction of a healthy volunteer. Overall, complex anatomical structure is better preserved in the QSM map by removing the chemical shift. There is a marked reduction of artifacts between fat and muscle, as indicated by the white arrows. Improved image contrast and clear delineations among prefemoral fat, cartilage, and muscle are observed.

The common peroneal nerve exhibits a diamagnetic susceptibility relative to its surroundings as shown in Fig. 5F. The susceptibility value of the peroneal nerve is −0.39 ± 0.06 ppm. Artery walls (red arrows in Fig. 5I), mostly comprising collagen, show a diamagnetic susceptibility with a value of −0.25 ± 0.14 ppm, while the blood appears relatively paramagnetic.

After removing the chemical shift effect, multilayered structures of articular cartilage are revealed by QSM (Fig. 6C) and they are compared to the R2* map (Fig. 6A). The susceptibility properties appear more diamagnetic (colored by blue) in the deep zone with a value of −0.07 ± 0.01 ppm, relatively less diamagnetic with a value of −0.01 ± 0.03 ppm in the middle zone, and relatively more paramagnetic with a value of 0.08 ± 0.02 ppm in the superficial zone (Fig. 6D).

Examples of the six ROIs, and their associated mean susceptibility values in the healthy volunteers, are given in Fig. 7A–B. Generally, the cartilage, muscle, and tibial nerve are more diamagnetic than fat pad, menisci, and subcutaneous fat which are relatively paramagnetic. The mean susceptibility values in all the volunteers are given in the Supporting Table. S1. The tibial nerve is significantly more diamagnetic than the muscle ($P < .001$) and the muscle is significantly more diamagnetic than cartilage with the $P < .001$. No significant difference was found between the fat pad and the menisci.

In patient #1, a posterior meniscal tear is detected by a hyperintensity on PD images as indicated by white arrow (Fig. 8D). This area is also visible in T2 FSE image (Fig. 8E), though the increased signal intensity is less clear than that of PD image. QSM imaging consistently shows a contour abnormality (more diamagnetic) in the same area compared with the surrounding meniscal tissue (Fig. 8F) as a result the contour of the triangle is missing compared to that of the healthy volunteer (Fig. 8C). Similar results are observed in patient #2 in which the anterior meniscal tear was detected. The more diamagnetic susceptibility caused by the tears may be related to the collagen orientation change within the menisci. Most of the collagen in the normal menisci are coherently orientated perpendicular to the B_0 field, thus exhibiting paramagnetic susceptibility. The tears/damage can disrupt these well-oriented collagen fibers and lead to a relatively random collagen fiber orientations, which causes susceptibility changes compared with the normal meniscal regions.

Abnormal areas in both femoral and tibial cartilages were detected by QSM in patient #1 54-year-old male), which shows that these areas exhibit more paramagnetic susceptibility (arrows in Fig. 9H) near the deep zone than that of the healthy subject (Fig. 9D). Mean susceptibility values in these areas are 0.45 ± 0.06 ppm (paramagnetic) which is much more

paramagnetic compared to those of healthy volunteers (around −0.1 ppm) in the deep zone. These areas are also identified on the R2* map as indicated by red and blue arrows in Fig. 9F. The increased R2* values in the focal area are consistent with a lower collagen density or collagen degeneration as collagen has shorter R2* relaxation rate (44). The contrast is higher on the QSM image (red arrow in Fig. 9H) than R2* map (red arrow in Fig. 9F). This suggests that QSM may be more sensitive to the degenerative articular cartilage disease than both GRE magnitude and R2* mapping (Fig. 9E–F). These medial abnormal areas are also clearly visible in the coronal orientation (Fig. 10). In addition, layer-specific contrast of the cartilage, which is clearly visible in QSM image in the normal lateral side cartilage, is lost in the abnormal medial side (Fig. 10).

Discussion

The results presented here indicate that QSM allows *in vivo* imaging and quantification of the magnetic susceptibility of the knee at high resolution and shows strong contrast between different tissues. High image quality is obtained due to both the chemical shift removal and improved QSM reconstruction algorithm with negligible streaking artifacts. First, a contrast pattern suggestive of an underlying layer structure is observed within the articular cartilage. Second, meniscal tears are detected using QSM. These preliminary findings demonstrate the promise of QSM to serve as a quantitative tool for evaluating various knee diseases.

One source of diamagnetic susceptibility may not act alone in producing the B_0 orientation-dependent susceptibility contrast in the cartilage. Other potential sources of anisotropy include proteoglycans, noncollagenous proteins and glycoproteins. Proteoglycans, including aggrecan, decorin, biglycan, and fibromodulin, represent the second-largest group of macromolecules in the extracellular matrix and account for 10% – 15% of the wet weight (35). The most abundant by weight is aggrecan that has more than 100 chondroitin sulfate and keratin sulfate chains. However, because sulfate constitutes such a small fraction of the cartilage relative to collagens, the susceptibility anisotropy of the collagen fibers appear to be more dominant. The TE dependence of magnetic susceptibility anisotropy can be attributed to multiple compartmentalized contributions to the signal from water pools experiencing different magnetic fields within the measured volume. Fig. 3D&F show that the apparent frequency of a complex average of intra-fibril and extra-fibril space strongly dependent on the fibril orientation relative to B_0 field. In addition, the apparent frequency of intra-fibril space varies with time. As shown by the signal magnitude decays in Fig. 3C&E, the intra-fibril space has a significant lower T2´ than extra-fibril space. In this case, spin dephasing and therefore signal attenuation in the intra-fibril region are faster, leaving the extra-fibril field perturbation to dominate the measured frequency and calculated susceptibility. Moreover, the susceptibility anisotropy in the extra-fibril space is larger than that of intra-fibril space where susceptibility anisotropy of collagen microfibrils may cancel each other. As a result, the complex average of distributed spins across the entire 3D frequency maps yielded a TE-dependent magnetic susceptibility anisotropy (Fig.3H&I). The current simulation model does not apply T_1 or T_2 weighting to the intra-fibril and extra-fibril volume signals. However, the model takes into account the T_2' decays that are inherently modeled due to the inhomogeneous magnetic fields within the simulated intra-fibril and extra-fibril volumes.

The characteristics of B_0 orientation-dependent R2* anisotropy have been investigated in brain white matter (45,46). In this study, an R2* anisotropy contrast weaker than susceptibility anisotropy was observed in the articular cartilage as shown in Fig. 4. Since R2* = R2 + R2′, one possible explanation for the weaker R2* anisotropy is that the R2 anisotropy and R2′ anisotropy have opposing signs and may cancel each other. Previous studies on orientation dependent T2 relaxation in cartilage shows that superficial zone has higher T2 than deep zone when the normal of specimen surface is parallel to B_0 (47). At this orientation, collagen fibrils are perpendicular and parallel to B_0 within the superficial zone and deep zone, respectively. On the other hand, as shown by our simulation results in Fig. 3G, T2′ is actually lower when collagen fibril is perpendicular to B_0 than that of parallel to B_0. Therefore, the B_0 orientation dependent T2 and T2′ anisotropy do cancel each other which results in a reduced B_0 field orientation dependence of T2* (or 1/R2*).

Cartilage exhibits a variation of susceptibility values from the superficial zone to the deep zone, with more diamagnetic tissue in the deep zone, approximately zero susceptibility in the middle zone, and paramagnetic tissue in the superficial zone. This spatial variation of the susceptibility as measured in cartilage is consistent with the simulation results as shown by the gray area in Fig. 3I. This regional variation on QSM images (Fig. 6D) is caused by the orientation of collagen fibrils within the cartilage (Fig. 6B) relative to B_0 field. When collagen fibrils are mostly parallel to B_0 field, the susceptibility values become more diamagnetic, e.g. in the deep zone. When collagen fibrils are mostly oriented perpendicular to B_0 field, the susceptibility values are more paramagnetic, e.g. in the superficial zone. Note this behavior of susceptibility anisotropy differs from that observed in brain white matter, in which myelinated axons appear more paramagnetic when parallel to B_0 field. This difference is due to the right-handed triple-helix structure of the collagen fiber. The planar peptide groups in the polyproline helix of collagen fiber have an out-of-plane susceptibility that is more diamagnetic than the in-plane susceptibilities (32,48).

The susceptibility values reported in Supporting Table. S1 show a large variation for similar fat tissues, e.g., 0.08 ppm in the fat pad and 0.45 ppm in the subcutaneous fat. This difference can be caused by the different portion of fibrous septa contained in the fat pad and subcutaneous fat, as well as their distributed orientations relative to B_0 field, which affect the measured susceptibility value averaged within each ROI. In addition, the shape and orientation of fat lobules separated by these fibrous septa, which may also affect the measured magnetic susceptibility.

The tibial nerve has diamagnetic susceptibility in the human knee. This diamagnetic susceptibility is determined by the basic unit of the peripheral nerve – myelination by Schwann cells and collagen supporting structures. Note that not all peripheral nerves are myelinated. Although imaging the peripheral nervous system is difficult, QSM may be useful for identifying and characterizing certain peripheral nerve pathology, e.g. nerve tumors.

The susceptibility difference between diamagnetic sciatic nerve (−0.39 ppm) and paramagnetic subcutaneous fat (0.45 ppm) is −0.84 ppm, which is comparable with susceptibility difference between white matter and fat tissue in brain reported by prior

literature (49,50). While the blood magnetic susceptibility in the knee artery should not be simply compared to the artery in brain which it may depend on the vessels orientation relative to the main field and blood oxygen level.

While our study has demonstrated the feasibility of high-resolution and high-contrast QSM of the knee joint at 7 T, more data is necessary to draw conclusions on its clinical utility in comparison with other techniques, e.g. T1ρ and T2 mapping. Nevertheless, QSM offers several clear technical advantages: reduced heating, less sensitivity to B_1 and B_0 inhomogeneity, and volumetric coverage at high resolution and throughput. Increased specific absorption rate (SAR) is a major concern at 7 T for both T1ρ and T2 mapping due to the use of high-energy RF pulses such as spin lock pulses and refocusing pulses; QSM, on the other hand, uses low-power small flip angle excitation pulses thus dramatically reducing SAR. Both B_1 and B_0 field inhomogeneity increase at 7 T and can substantially affect the quantification of T1ρ and T2 relaxation times; QSM, on the other hand, has limited sensitivity to B_1 inhomogeneity and in fact benefits from increased contrast due to the higher B_0 field. Shorter T2* relaxation and higher phase contrast-to-noise ratio at 7 T allows QSM to be acquired rapidly with the robust GRE sequence using a relatively short TR. The entire QSM study protocol can be performed within 17 minutes at a resolution of 0.4×0.4×1.6 mm^3 covering the entire knee.

One limitation of this study is that susceptibility of bone and marrow cannot be depicted. The phase of bone is not accurately available since the T2* relaxation of the bone and marrow is much shorter in comparison to surrounding soft tissues at 7 T. In the current study, the bone areas are masked out in order to prevent inaccurate estimation of the field map, which would introduce errors due to the ill-posed inverse problem. Future studies employing ultrashort TE pulse sequences can be used for imaging magnetic susceptibility of bone and marrow (20).

Conclusions

In this study we have successfully demonstrated the feasibility of quantifying susceptibility of the human knee joint *in vivo* at 7 T. The multilayered structures of articular cartilage is demonstrated by QSM. QSM is able to probe meniscal tears and demonstrates a visible contrast change of degenerative cartilage. These results suggest that QSM may be sensitive to early knee disease detection, which is useful for treatment and the evaluation of disease progression.

Supplementary Material

Refer to Web version on PubMed Central for supplementary material.

Acknowledgments

The authors thank Matthew Cronin and Eric Gibbs for their careful proofreading of our manuscript. This study was supported in part by the National Institutes of Health through grants NIMH R01MH096979 and NINDS R01NS079653.

References

1. Haacke E, Tang J, Neelavalli J, Cheng Y. Susceptibility mapping as a means to visualize veins and quantify oxygen saturation. Journal of Magnetic Resonance Imaging. 2010; 32(3):663–676. [PubMed: 20815065]
2. Schweser F, Deistung A, Lehr BW, Reichenbach JR. Quantitative imaging of intrinsic magnetic tissue properties using MRI signal phase: an approach to in vivo brain iron metabolism? Neuroimage. 2011; 54(4):2789–2807. [PubMed: 21040794]
3. Shmueli K, de Zwart JA, van Gelderen P, Li TQ, Dodd SJ, Duyn JH. Magnetic susceptibility mapping of brain tissue in vivo using MRI phase data. Magnetic Resonance in Medicine. 2009; 62(6):1510–1522. [PubMed: 19859937]
4. Li L, Leigh JS. Quantifying arbitrary magnetic susceptibility distributions with MR. Magnetic resonance in medicine. 2004; 51(5):1077–1082. [PubMed: 15122694]
5. de Rochefort L, Liu T, Kressler B, Liu J, Spincemaille P, Lebon V, Wu J, Wang Y. Quantitative susceptibility map reconstruction from MR phase data using bayesian regularization: validation and application to brain imaging. Magnetic Resonance in Medicine. 2010; 63(1):194–206. [PubMed: 19953507]
6. Wharton S, Schäfer A, Bowtell R. Susceptibility mapping in the human brain using threshold-based k-space division. Magnetic resonance in medicine. 2010; 63(5):1292–1304. [PubMed: 20432300]
7. Carpenter KL, Li W, Wei H, Wu B, Xiao X, Liu C, Worley G, Egger HL. Magnetic susceptibility of brain iron is associated with childhood spatial IQ. NeuroImage. 2016; 132:167–174. [PubMed: 26899787]
8. Cronin MJ, Wharton S, Al-Radaideh A, Constantinescu C, Evangelou N, Bowtell R, Gowland PA. A comparison of phase imaging and quantitative susceptibility mapping in the imaging of multiple sclerosis lesions at ultrahigh field. Magnetic Resonance Materials in Physics, Biology and Medicine. 2016:1–15.
9. Li X, Vikram DS, Lim IAL, Jones CK, Farrell JA, van Zijl PC. Mapping magnetic susceptibility anisotropies of white matter in vivo in the human brain at 7T. Neuroimage. 2012; 62(1):314–330. [PubMed: 22561358]
10. Liu C. Susceptibility tensor imaging. Magnetic resonance in medicine. 2010; 63(6):1471–1477. [PubMed: 20512849]
11. Wharton S, Bowtell R. Fiber orientation-dependent white matter contrast in gradient echo MRI. Proceedings of the National Academy of Sciences. 2012; 109(45):18559–18564.
12. Xie L, Dibb R, Cofer GP, Li W, Nicholls PJ, Johnson GA, Liu C. Susceptibility tensor imaging of the kidney and its microstructural underpinnings. Magnetic resonance in medicine. 2015; 73(3): 1270–1281. [PubMed: 24700637]
13. Dibb R, Qi Y, Liu C. Magnetic susceptibility anisotropy of myocardium imaged by cardiovascular magnetic resonance reflects the anisotropy of myocardial filament α-helix polypeptide bonds. Journal of Cardiovascular Magnetic Resonance. 2015; 17(1):1. [PubMed: 25589308]
14. Dibb R, Xie L, Wei H, Liu C. Magnetic susceptibility anisotropy outside the central nervous system. NMR in Biomedicine. 2016
15. Deistung A, Schweser F, Wiestler B, Abello M, Roethke M, Sahm F, Wick W, Nagel AM, Heiland S, Schlemmer H-P. Quantitative susceptibility mapping differentiates between blood depositions and calcifications in patients with glioblastoma. PloS one. 2013; 8(3):e57924. [PubMed: 23555565]
16. Chen W, Zhu W, Kovanlikaya I, Kovanlikaya A, Liu T, Wang S, Salustri C, Wang Y. Intracranial calcifications and hemorrhages: characterization with quantitative susceptibility mapping. Radiology. 2014; 270(2):496–505. [PubMed: 24126366]
17. Wei H, Xie L, Dibb R, Li W, Decker K, Zhang Y, Johnson GA, Liu C. Imaging whole-brain cytoarchitecture of mouse with MRI-based quantitative susceptibility mapping. NeuroImage. 2016; 137:107–115. [PubMed: 27181764]
18. Wei, H., Wang, B., Zong, X., Lin, W., Wang, N., Liu, C. Proc Intl Soc Mag Reson Med. Toronto, ON, Canada: 2015. Imaging magnetic susceptibility of the human knee joint at 3 and 7 Tesla; p. 288

19. Khalidov, I., Liu, T., Prince, M., Wang, Y. Proc Intl Soc Mag Reson Med. Montréal, Québec, Canada: 2011. Susceptibility mapping: computatio n of the field map using water-fat separation at 7T; p. 4475
20. Dimov, AV., Liu, Z., Spincemaille, P., Du, J., Wang, Y. Proc Intl Soc Mag Reson Med. Toronto, ON, Canada: 2015. Quantitative susceptibility mapping of bone using ultra-short TE sequence; p. 0938
21. Wang L, Nissi MJ, Toth F, Johnson CP, Garwood M, Carlson CS, Ellermann J. Quantitative susceptibility mapping detects abnormalities in cartilage canals in a goat model of preclinical osteochondritis dissecans. Magnetic resonance in medicine. 2016
22. Nissi MJ, Tóth F, Wang L, Carlson CS, Ellermann JM. Improved visualization of cartilage canals using quantitative susceptibility mapping. PloS one. 2015; 10(7):e0132167. [PubMed: 26168296]
23. Bittersohl B, Hosalkar HS, Hughes T, Kim YJ, Werlen S, Siebenrock KA, Mamisch TC. Feasibility of T 2* mapping for the evaluation of hip joint cartilage at 1.5 T using a three-dimensional (3D), gradient-echo (GRE) sequence: A prospective study. Magnetic Resonance in Medicine. 2009; 62(4):896–901. [PubMed: 19645008]
24. Filidoro L, Dietrich O, Weber J, Rauch E, Oerther T, Wick M, Reiser M, Glaser C. High-resolution diffusion tensor imaging of human patellar cartilage: Feasibility and preliminary findings. Magnetic Resonance in Medicine. 2005; 53(5):993–998. [PubMed: 15844163]
25. Li X, Ma CB, Link TM, Castillo D-D, Blumenkrantz G, Lozano J, Carballido-Gamio J, Ries M, Majumdar S. In vivo T 1ρ and T 2 mapping of articular cartilage in osteoarthritis of the knee using 3T MRI. Osteoarthritis and cartilage. 2007; 15(7):789–797. [PubMed: 17307365]
26. Brandt K, Radin E, Dieppe P, Van De Putte L. Yet more evidence that osteoarthritis is not a cartilage disease. Annals of the Rheumatic Diseases. 2006; 65(10):1261–1264. [PubMed: 16973787]
27. Liu C, Wei H, Gong N-J, Cronin M, Dibb R, Decker K. Quantitative Susceptibility Mapping: Contrast Mechanisms and Clinical Applications. TOMOGRAPHY. 2015; 1(1):3–17. [PubMed: 26844301]
28. Bao L, Li X, Cai C, Chen Z, van Zijl P. Quantitative Susceptibility Mapping using Structural Feature based Collaborative Reconstruction (SFCR) in the Human Brain. 2016
29. Liu C, Li W, Tong KA, Yeom KW, Kuzminski S. Susceptibility-weighted imaging and quantitative susceptibility mapping in the brain. Journal of Magnetic Resonance Imaging. 2014; 42(2):23–41. [PubMed: 25270052]
30. Sharma SD, Hernando D, Horng DE, Reeder SB. Quantitative susceptibility mapping in the abdomen as an imaging biomarker of hepatic iron overload. Magnetic resonance in medicine. 2015; 74(3):673–683. [PubMed: 25199788]
31. Dong J, Liu T, Chen F, Zhou D, Dimov A, Raj A, Cheng Q, Spincemaille P, Wang Y. Simultaneous phase unwrapping and removal of chemical shift (SPURS) using graph cuts: application in quantitative susceptibility mapping. IEEE transactions on medical imaging. 2015; 34(2):531–540. [PubMed: 25312917]
32. Worcester D. Structural origins of diamagnetic anisotropy in proteins. Proceedings of the National Academy of Sciences. 1978; 75(11):5475–5477.
33. Shoulders MD, Raines RT. Collagen structure and stability. Annual review of biochemistry. 2009; 78:929.
34. Holmes DF, Kadler KE. The 10+ 4 microfibril structure of thin cartilage fibrils. Proceedings of the National Academy of Sciences. 2006; 103(46):17249–17254.
35. Knupp C, Squire JM. Molecular packing in network-forming collagens. Advances in protein chemistry. 2005; 70:375–403. [PubMed: 15837521]
36. Pauling L. Diamagnetic anisotropy of the peptide group. Proceedings of the National Academy of Sciences. 1979; 76(5):2293–2294.
37. Chu K, Xu Y, Balschi JA, Springer CS. Bulk magnetic susceptibility shifts in NMR studies of compartmentalized samples: use of paramagnetic reagents. Magnetic resonance in medicine. 1990; 13(2):239–262. [PubMed: 2156125]
38. Li W, Wu B, Avram AV, Liu C. Magnetic susceptibility anisotropy of human brain in vivo and its molecular underpinnings. Neuroimage. 2012; 59(3):2088–2097. [PubMed: 22036681]

39. Liu T, Khalidov I, de Rochefort L, Spincemaille P, Liu J, Tsiouris AJ, Wang Y. A novel background field removal method for MRI using projection onto dipole fields (PDF). NMR in Biomedicine. 2011; 24(9):1129–1136. [PubMed: 21387445]
40. Wei H, Dibb R, Zhou Y, Sun Y, Xu J, Wang N, Liu C. Streaking artifact reduction for quantitative susceptibility mapping of sources with large dynamic range. NMR in Biomedicine. 2015; 28(10): 1294–1303. [PubMed: 26313885]
41. Yushkevich PA, Piven J, Hazlett HC, Smith RG, Ho S, Gee JC, Gerig G. User-guided 3D active contour segmentation of anatomical structures: significantly improved efficiency and reliability. Neuroimage. 2006; 31(3):1116–1128. [PubMed: 16545965]
42. Reeder SB, Pineda AR, Wen Z, Shimakawa A, Yu H, Brittain JH, Gold GE, Beaulieu CH, Pelc NJ. Iterative decomposition of water and fat with echo asymmetry and least-squares estimation (IDEAL): application with fast spin-echo imaging. Magnetic resonance in medicine. 2005; 54(3): 636–644. [PubMed: 16092103]
43. Wei H, Zhang Y, Gibbs E, Chen NK, Wang N, Liu C. Joint 2D and 3D phase processing for quantitative susceptibility mapping: application to 2D echo-planar imaging. NMR in Biomedicine. 2016 Epub ahead of print.
44. Bittersohl B, Miese F, Hosalkar H, Herten M, Antoch G, Krauspe R, Zilkens C. T2* mapping of hip joint cartilage in various histological grades of degeneration. Osteoarthritis and Cartilage. 2012; 20(7):653–660. [PubMed: 22469845]
45. Lee J, van Gelderen P, Kuo L-W, Merkle H, Silva AC, Duyn JH. T 2*-based fiber orientation mapping. Neuroimage. 2011; 57(1):225–234. [PubMed: 21549203]
46. Lee J, Nam Y, Choi JY, Kim EY, Oh SH, Kim DH. Mechanisms of T2* anisotropy and gradient echo myelin water imaging. NMR in Biomedicine. 2016
47. Xia Y, Moody JB, Alhadlaq H. Orientational dependence of T2 relaxation in articular cartilage: A microscopic MRI (μMRI) study. Magnetic resonance in medicine. 2002; 48(3):460–469. [PubMed: 12210910]
48. Torbet J, Ronziere M-C. Magnetic alignment of collagen during self-assembly. Biochem j. 1984; 219:1057–1059. [PubMed: 6743242]
49. Buch S, Liu S, Ye Y, Cheng YCN, Neelavalli J, Haacke EM. Susceptibility mapping of air, bone, and calcium in the head. Magnetic resonance in medicine. 2015; 73(6):2185–2194. [PubMed: 25046134]
50. Liu Z, Kee Y, Zhou D, Wang Y, Spincemaille P. Preconditioned total field inversion (TFI) method for quantitative susceptibility mapping. Magnetic Resonance in Medicine. 2016
51. Magnusson S, Hansen P, Kjaer M. Tendon properties in relation to muscular activity and physical training. Scandinavian journal of medicine & science in sports. 2003; 13(4):211–223. [PubMed: 12859603]

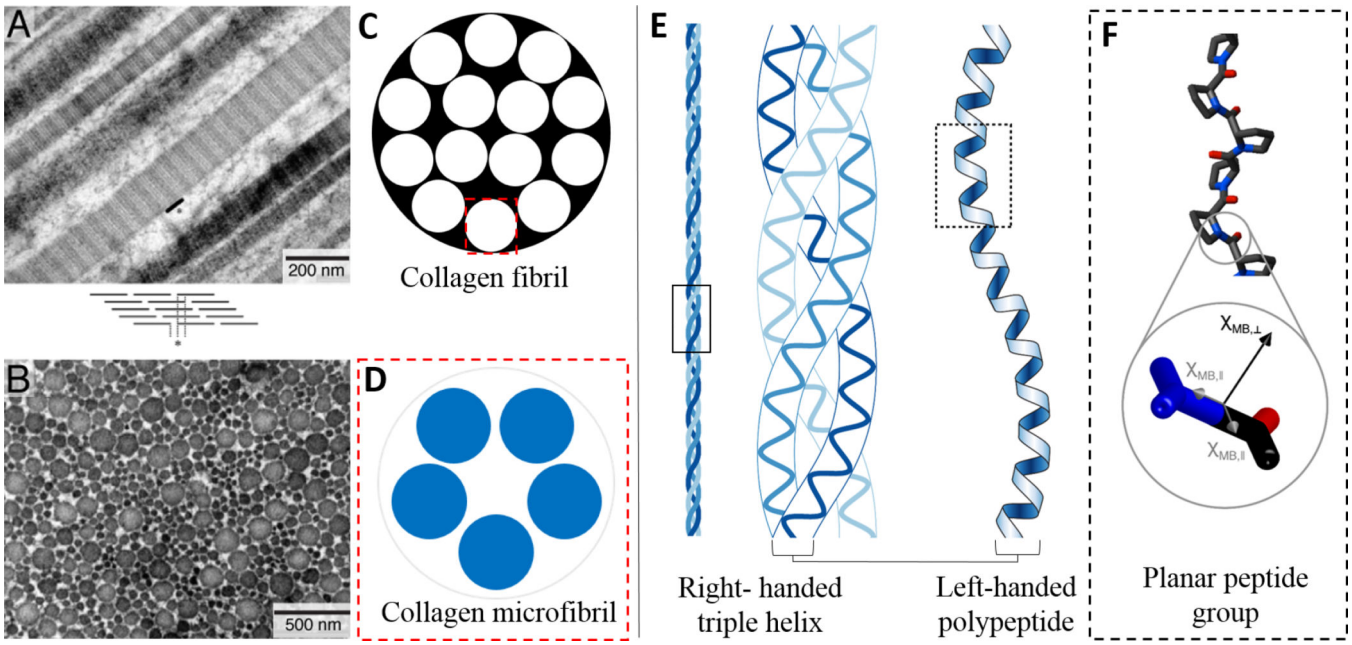

Figure 1.

Microstructural basis of the collagen model. (A, B) Electron microscopy of longitudinal and axial sections of human Achilles tendon fibrils (images used with permission from Magnusson (51)). The black marker (*) in (A) corresponds to the length of one repeating collagen fibril. (C) A collagen fibril is composed of fourteen microfibrils. (D) A zoomed-in view of the dashed red line rectangle from C shows the collagen microfibrillar structure which is composed of five right-handed triple helices. (E) Right-handed triple helix and left-handed polypeptide structure. A zoomed-in view of the solid rectangle shows the detailed structure of the right-handed triple helix structure. (F) Magnification of the area outlined in black dotted rectangle on the left-handed polypeptide shows the detailed planar peptide groups, which have an out-of-plane susceptibility (black arrow) that is more diamagnetic than in-plane susceptibility (gray arrows).

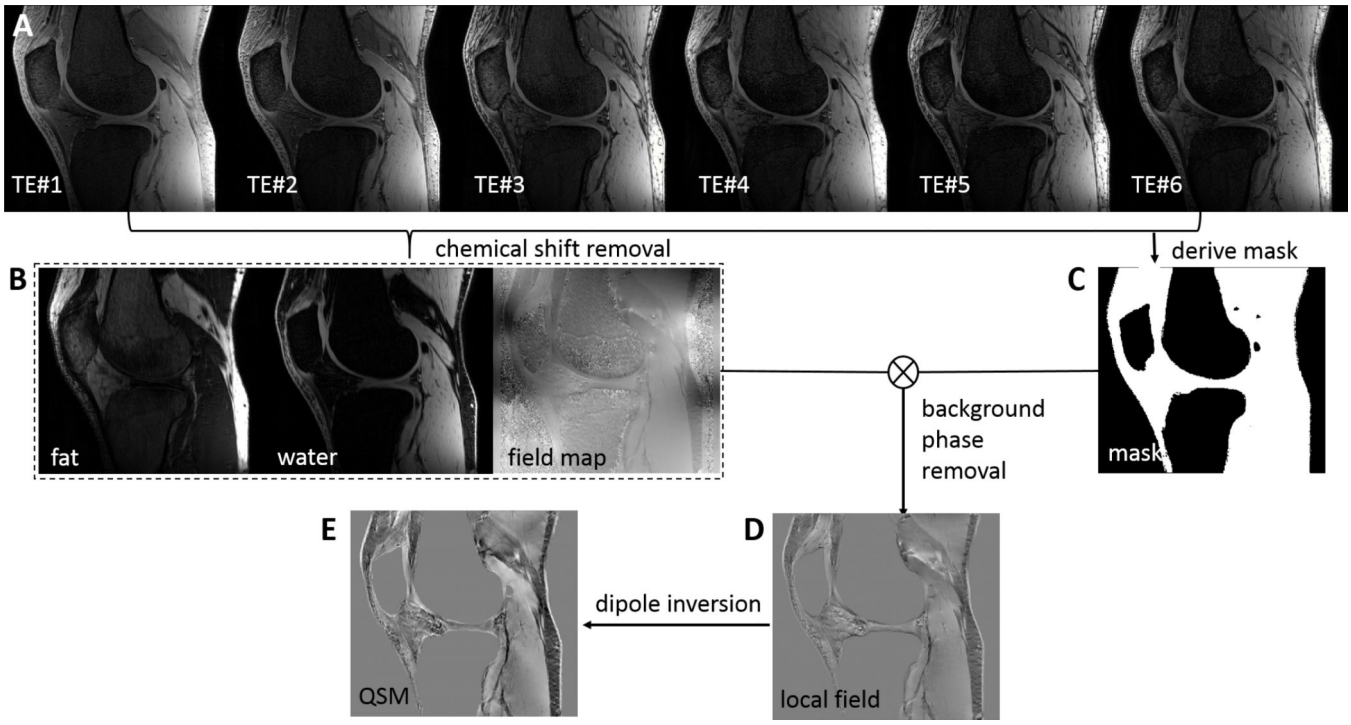

Figure 2.

Processing pipeline to estimate the susceptibility map of knee. Complex multi-echo images (A) are used to estimate the B_0 field map, water, and fat images (B). A knee mask (C) is derived from the magnitude image. The local field (D) is obtained by removing the background field using projection onto dipole field (PDF) or other methods. The QSM (E) was reconstructed by using STAR-QSM (streaking artifact reduction for QSM) method.

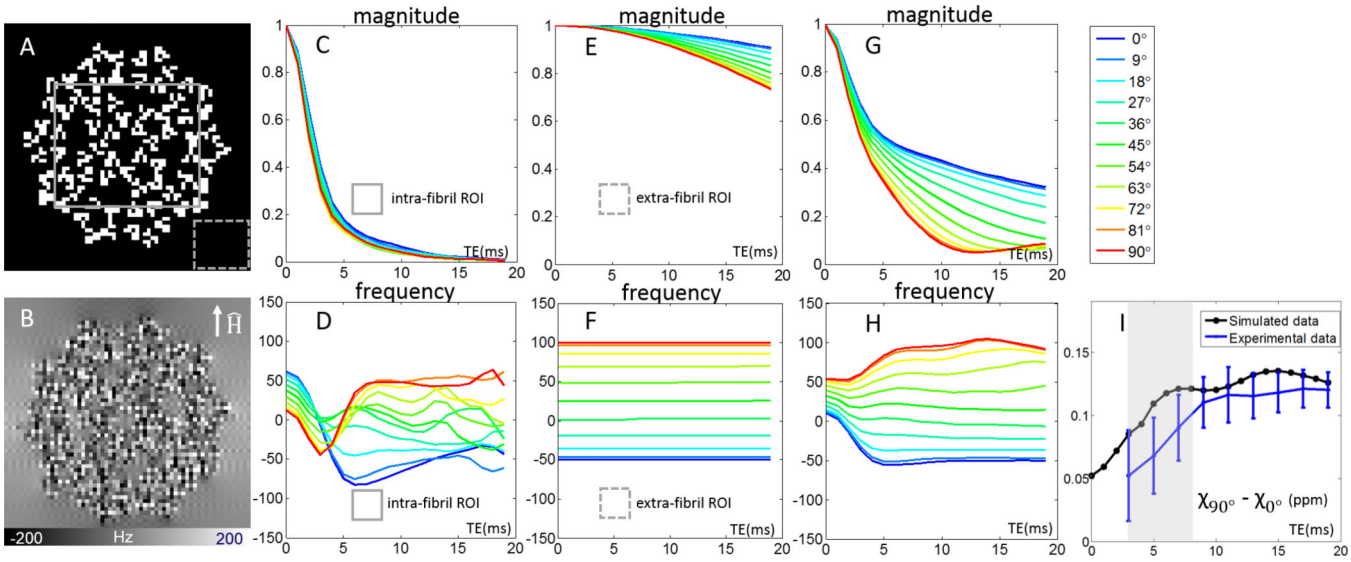

Figure 3.

(A) Cross section of 10+4 collagen model represented by a binary mask. (B) A simulated frequency map at 9.4 T calculated with collagen fibrils orientation perpendicular to $\hat{H}$. Mean apparent frequency and magnitude within intra-fibril ROI represented by solid gray rectangle (C, D), within extra-fibril ROI represented by dashed gray rectangle (E, F), and within the simulated volume (G, H) at different fibril orientations relative to B_0 field are plotted over echo time. (I) Comparison the susceptibility anisotropy between simulated data and experimental data. The experimental data were acquired on the *ex vivo* animal specimen at 9.4 T. Gray area in (I) indicates the TE range used in the *in vivo* human knee 3D GRE scans. The experimental data are displayed as mean ± standard deviation.

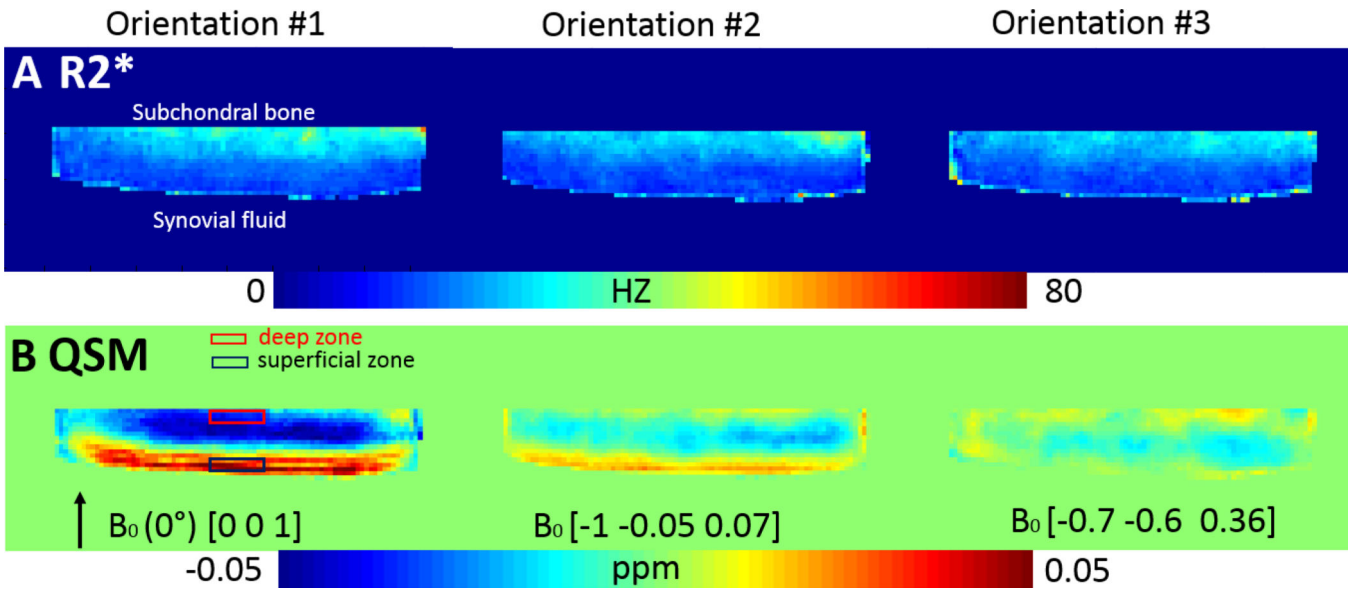

Figure 4.

B_0 field-orientation dependent modulation of R2* and magnetic susceptibility contrast in the cartilage by the *ex vivo* experimental data. The susceptibility of the collagen in different cartilage layers varies markedly from one orientation to another. Contrarily, the R2* contrast reveals a relatively small B_0 field-orientation dependence. The $\hat{\mathbf{H}}$ vectors for the three acquisitions were: (0, 0, 1), (−1, −0.05, 0.07) and (−0.7, −0.6, 0.36), which corresponds to 0°, 86° and 69° referenced to the normal of the articular surface, respectively

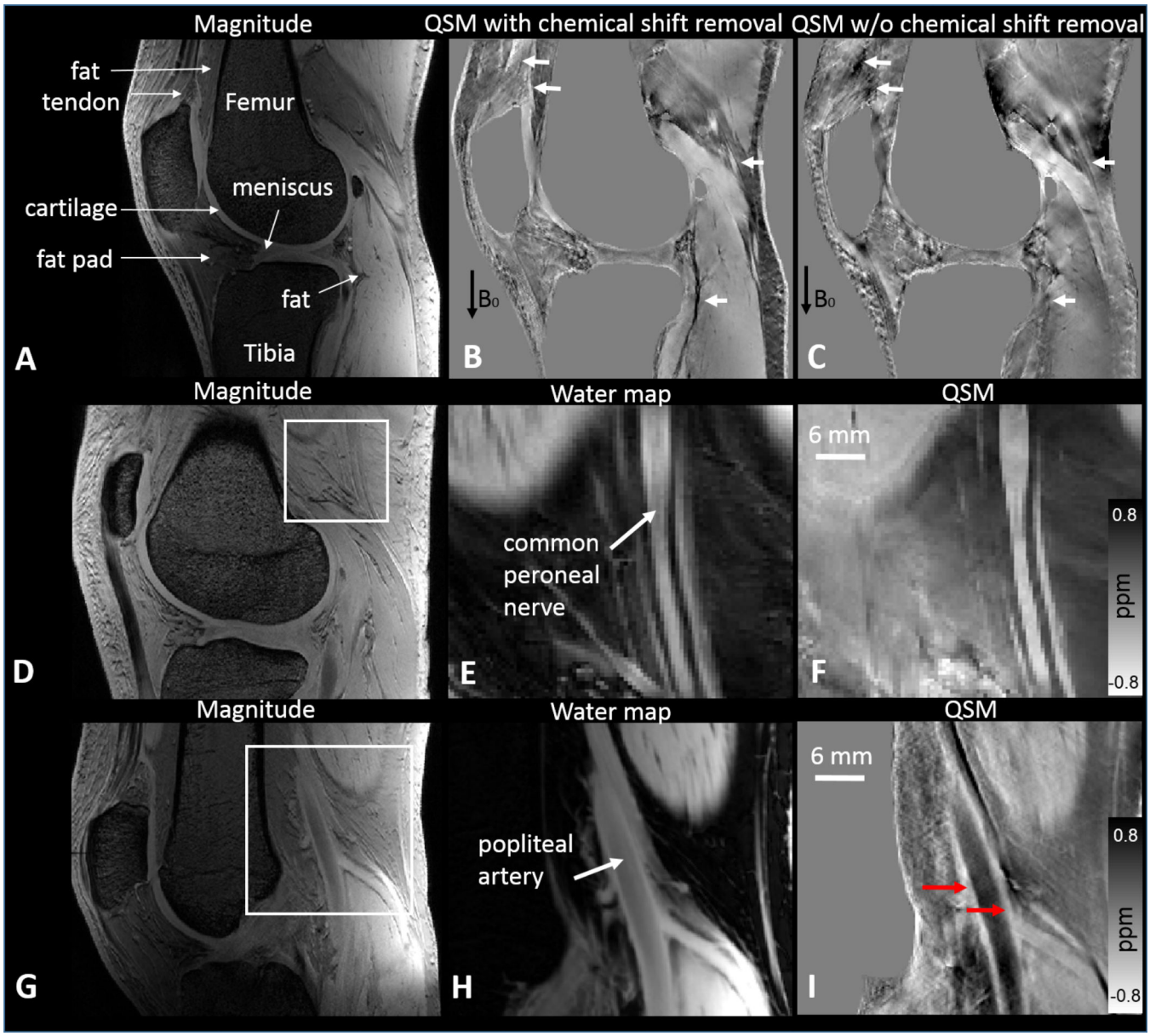

Figure 5.

Sagittal GRE images from the knee in healthy 38-year-old male. (A) Magnitude, (B) QSM with and (C) QSM without chemical shift removal. (E) Estimated water and (F) reconstructed susceptibility maps corresponding to the area outlined in the white box on (D) the magnitude image. Both water and QSM maps identify a portion of the common peroneal nerve just behind the knee. (G) Magnitude, (H) estimated water and (I) QSM map show the structure of the popliteal artery. Red arrows indicate the artery wall revealed by QSM.

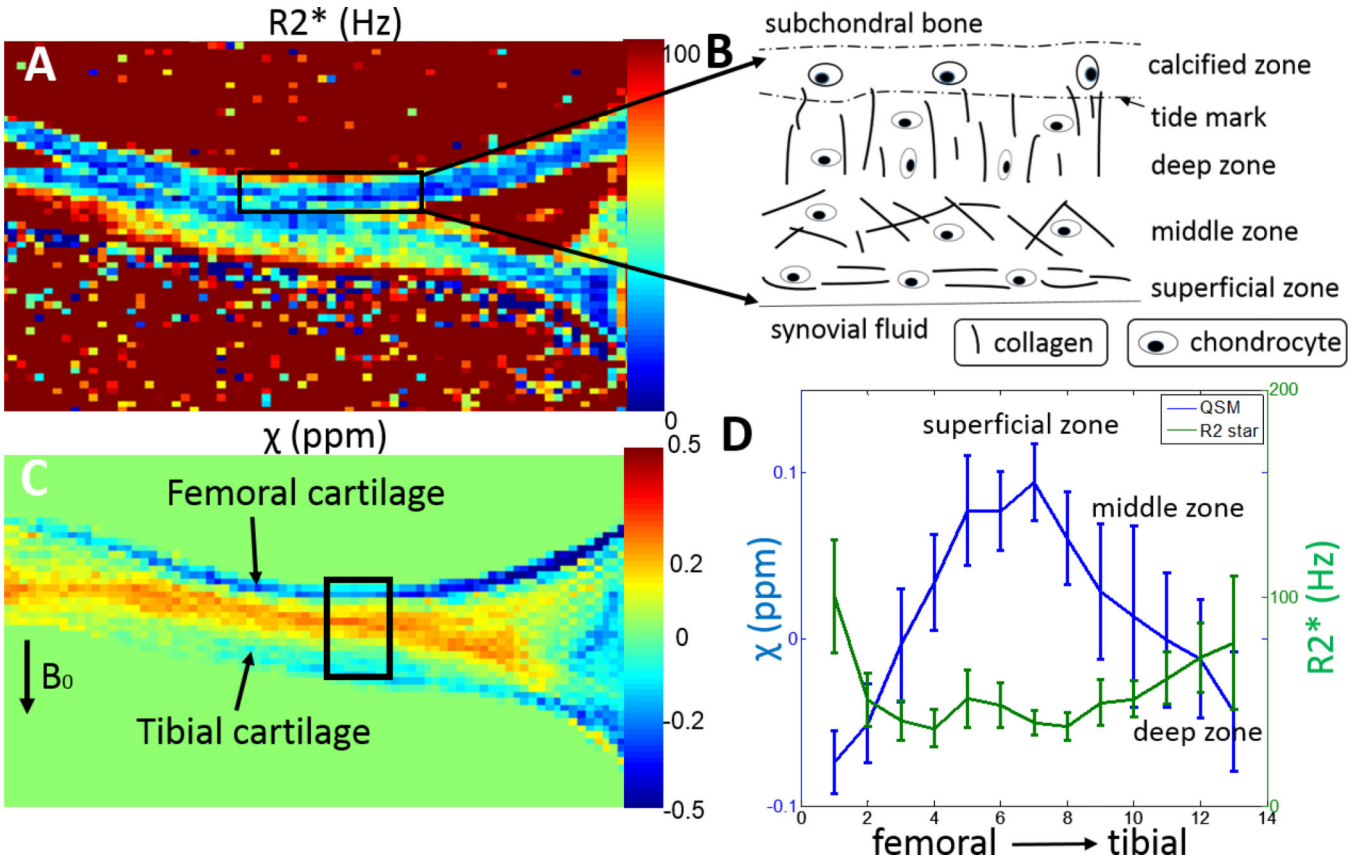

Figure 6.

Color maps of (A) R2* and (C) susceptibility (χ) in articular cartilage. (B) A schematic diagram represents the arrangements of collagen at different depths in the articular cartilage. (D) Susceptibility and R2* values plotted along the vertical positions from femoral to tibial cartilages within the black box in (C). The size of the box is 13 × 10 (row × column). The labels on the horizontal axis of (D) represents the voxel (row) number from femur bone surface to tibia bone surface. Error bars represent the standard deviation in each row (across 10 column).

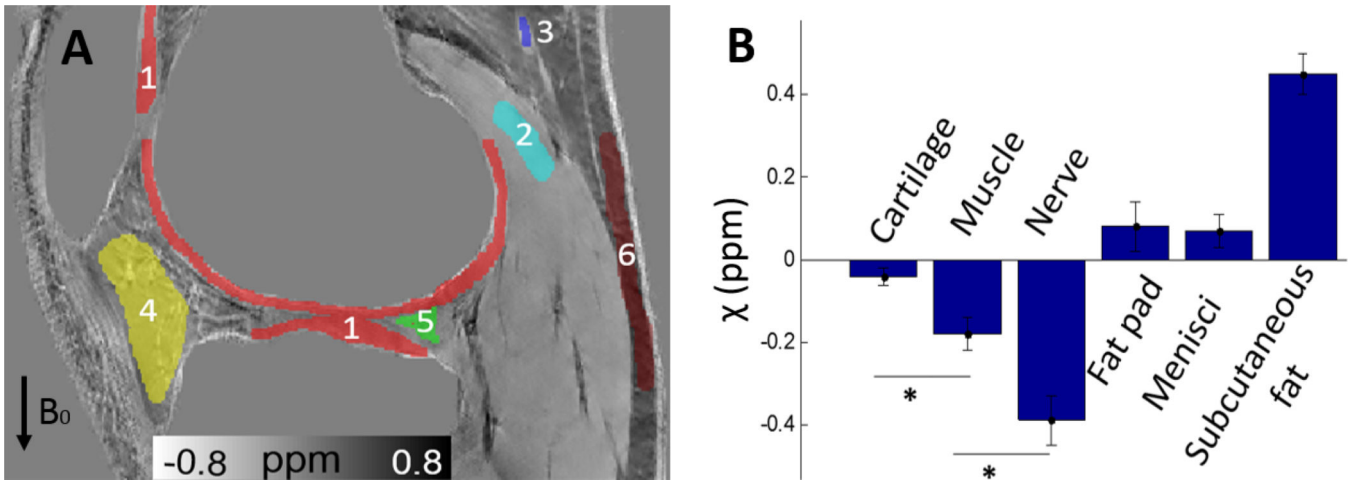

Figure 7.

Regions of interest (ROIs) and mean susceptibility for different specific tissue structures, 1. Cartilage; 2. Muscle; 3. Tibial nerve; 4. Fat pad; 5. Menisci; 6. Subcutaneous fat. (*P < .05)

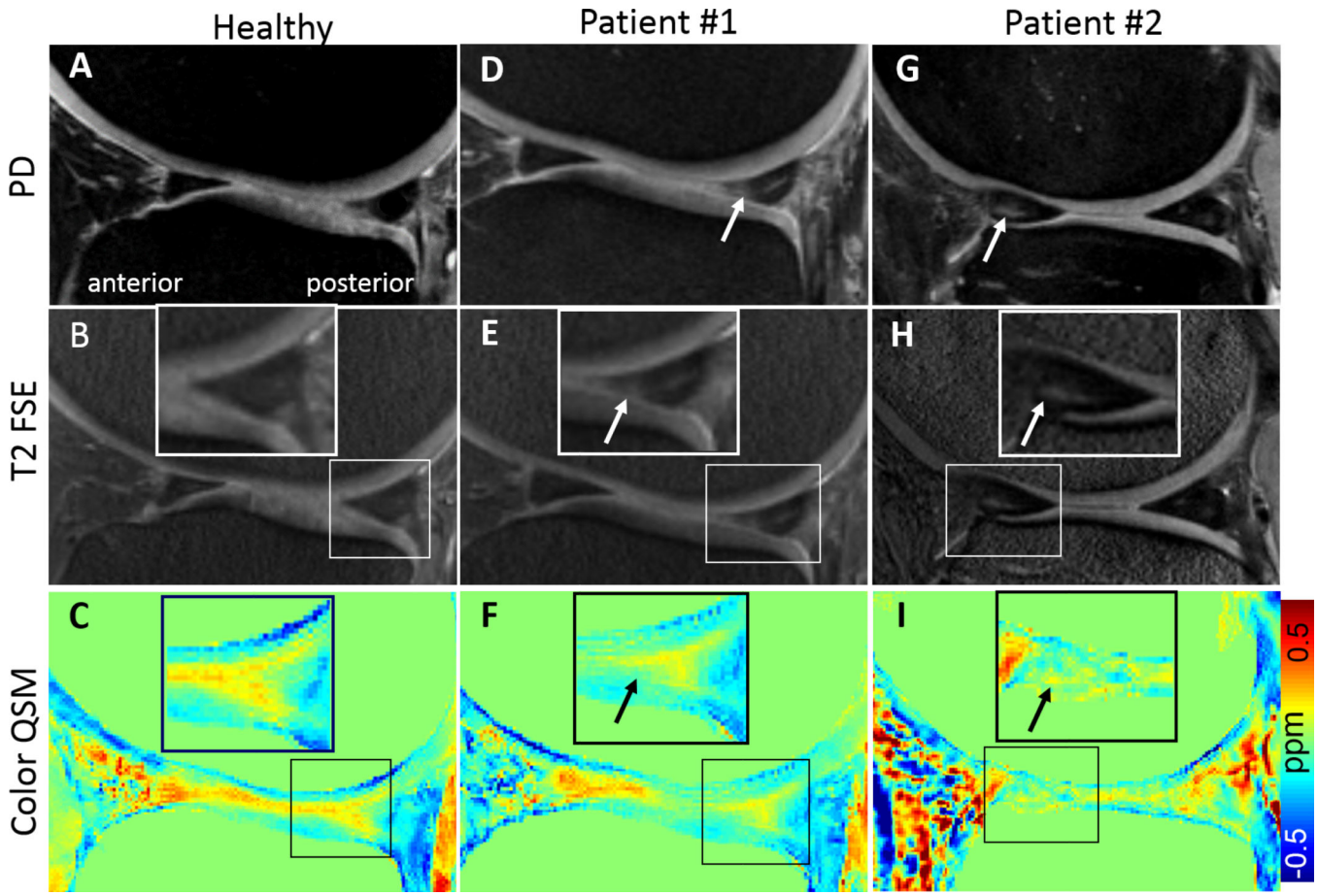

Figure 8.

Representative MRI images show two patients with meniscal tear (D–I) compared with a healthy subject (A–C). (D) Proton density (PD) image shows an area of hyperintense signal (arrow). (E) T2 FSE images also shows hyperintensity at the same location. (F) Color QSM maps show findings consistent with PD and T2 FSE images. It is shown that the triangle shape of the meniscus is smeared or missing as indicated by the arrows in zoomed-in view and the susceptibility values become more diamagnetic compared with the normal meniscal tissue (C). Similar results are found in anterior meniscus in Patient #2.

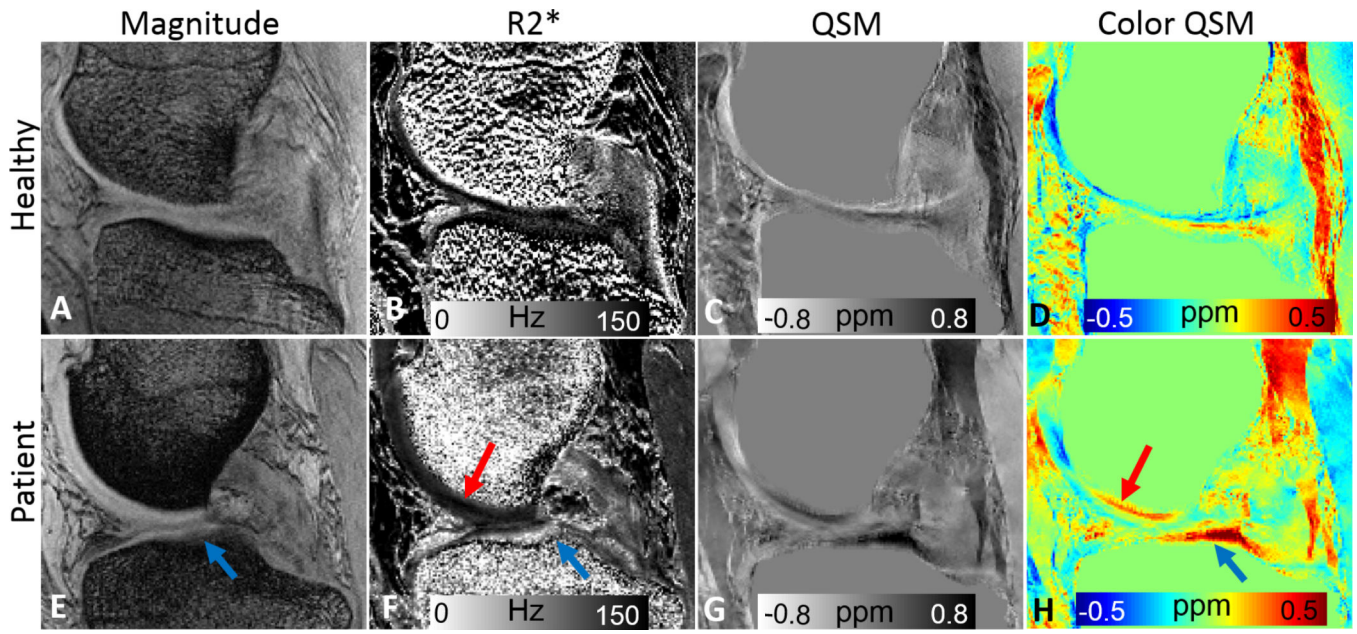

Figure 9.

Representative MRI images show medial cartilage in (A–D) a healthy subject, (E–H) patient #1 with collagen damage or degeneration. (A, E) GRE magnitude images show morphology of the cartilage. The cartilage appears normal in (A), but shows a decreased signal intensity in the tibial plateau (E). Corresponding R2* (B, F), QSM (C, G), and color QSM (D, H) maps clearly show difference in the cartilage between the healthy subject and the patient.

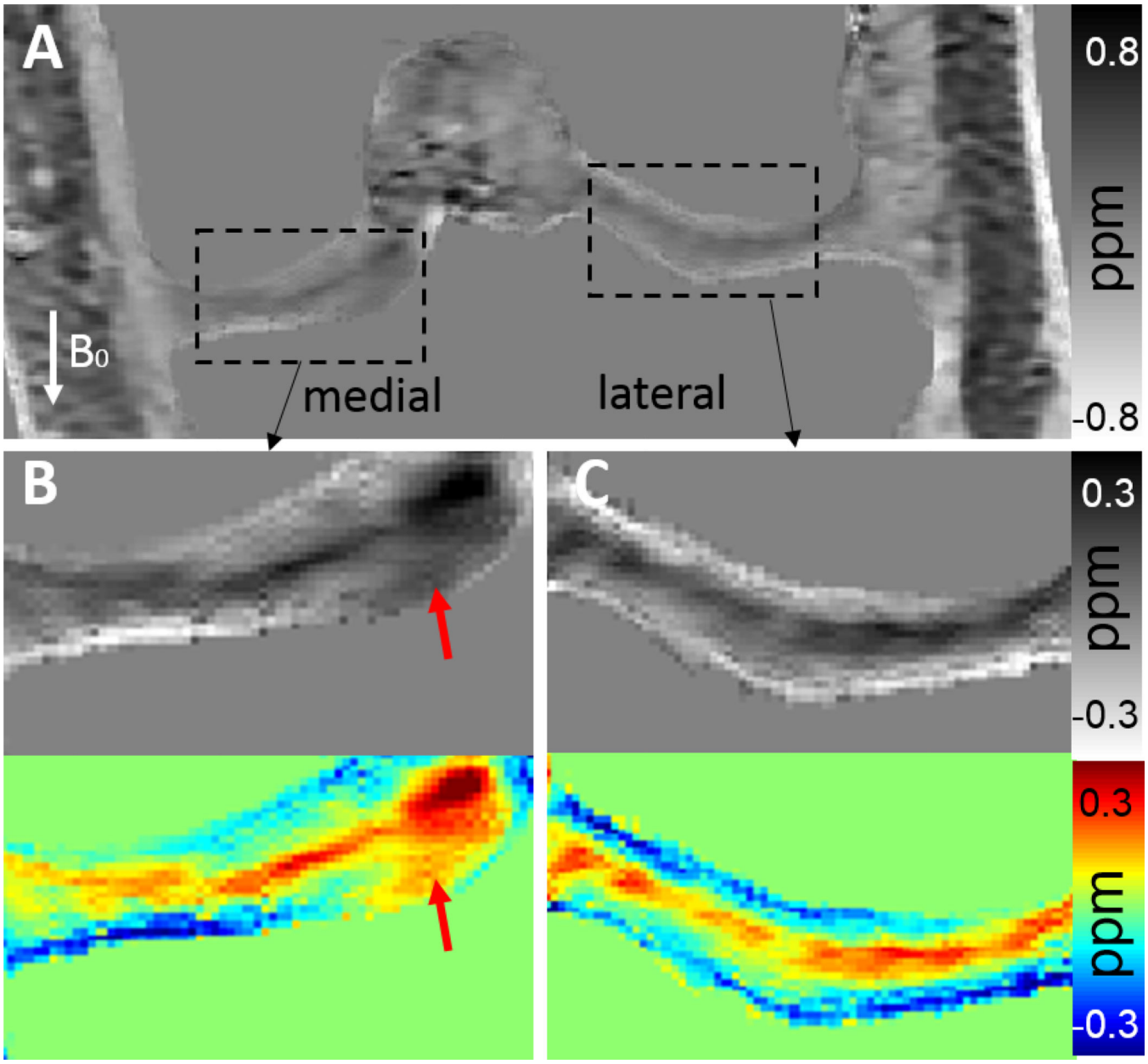

Figure 10.

(A) Cropped QSM image of cartilage in coronal orientation of patient #1. Rectangular boxes with dash lines correspond to medial and lateral cartilages. (B–C) Magnifications of the area outlined in black boxes from the medial and lateral cartilages, respectively, by both grayscale and color maps. Arrows indicate the deep zone of medial side tibial cartilage (B) with paramagnetic susceptibility compared with normal diamagnetic lateral side (C). The displayed coronal images were obtained by zero padding in k-space to interpolate to an isotropic resolution of $0.4 \times 0.4 \times 0.4\ mm^3$.